electronics

MDPI

Article

Thermal Analyses of Reactor under High-Power and High-Frequency Square Wave Voltage Based on Improved Thermal Network Model

Li Shen, Fan Xie *, Wenxun Xiao, Huayu Ji and Bo Zhang

School of Electric Power, South China University of Technology, Guangzhou 510000, China;
201920113774@mail.scut.edu.cn (L.S.); xiaowx@scut.edu.cn (W.X.);
201920113761@mail.scut.edu.cn (H.J.); epbzhang@scut.edu.cn (B.Z.)
* Correspondence: epfxie@scut.edu.cn; Tel.: +86-020-8711-1764

Abstract: In order to quickly calculate the stable temperature of a reactor driven by high-frequency and high-power pulse voltage, an improved thermal network model suitable for a reactor under this condition is established in this paper. In power electronic equipment, the maximum temperature of the reactor is usually concentrated in its internal core. Moreover, with the increasing demand of high-power density in power electronic devices, the structure design of the reactor is more compact, and the internal magnetic field will affect the accuracy of the temperature-measuring device. Therefore, it is difficult to measure the internal temperature rise of the reactor directly. However, its stable operating temperature could be analyzed by the thermal network modeling methods and heat transfer analysis tool. Therefore, a convenient and accurate thermal network model of the reactor under high-frequency and high-power square wave voltage is established by considering the equivalent thermal resistance of the winding, the three-dimensional geometrical effect of the core and the effect of the high-frequency repeated pulse stress on the thermal penetration depth. Additionally, the internal temperature of the reactor can be obtained through the external temperature in terms of the presented model. To verify the feasibility of the thermal network model, the corresponding multiphysical field finite element simulation and the reactor temperature measurement platform is built. The simulation and experimental results show that the proposed thermal network model has a high precision and fast calculation speed, and it is an effective tool for thermal analysis of the reactor.

Keywords: thermal network model; optical fiber temperature measuring; multiphysical field finite element model; high-frequency and high-power reactor

check for updates

Citation: Shen, L.; Xie, F.; Xiao, W.; Ji, H.; Zhang, B. Thermal Analyses of Reactor under High-Power and High-Frequency Square Wave Voltage Based on Improved Thermal Network Model. *Electronics* **2021**, *10*, 1342. https://doi.org/10.3390/electronics10111342

Academic Editors: Ali Cemal Benim and Barış Burak Kanbur

Received: 24 May 2021
Accepted: 1 June 2021
Published: 3 June 2021

1. Introduction

Currently, high-power electronic equipment is essential for the smart grid and new energy power generation. Hence, the safe and reliable operation of high-power electronic equipment has an increasingly significance on power grid security [1]. Among high-power electronic equipment, the high-frequency and high-power reactor is the link of power transmission between the converter and AC system and plays the role of controlling power transmission, filtering, restraining current fluctuation, restraining the circulation and preventing the current from rising fast during short circuit [2]. Therefore, the overall performance of the high-power electronic converter is highly dependent on the reactor, and it is vital to make a detailed thermal analysis of it. As shown in Figure 1, the typical winding voltage waveform of the high-frequency reactor is not a standard sine wave but has a complex frequency harmonic of square wave, along with a rapid rise, serious distortion and abnormal peak. The main reasons of this phenomenon are the influence of the leakage inductance and distributed capacitance, and them also causes additional core loss and winding loss [3]. Under this high-frequency electrical stress, the thermal and mechanical stress have additional influences on the heating of the reactor, which makes the operating temperature of the reactor more important. Moreover, under high-frequency conditions, the edges and corners of the magnetic core with significant magnetic field change will produce a very serious edge effect, resulting in serious heating, uneven temperature distribution and insulation failure. In addition, the temperature hot spots of the reactor are often concentrated in its interior, but the temperature sensor is difficult to measure directly. Therefore, effective thermal analyses are essential to solve this issue.

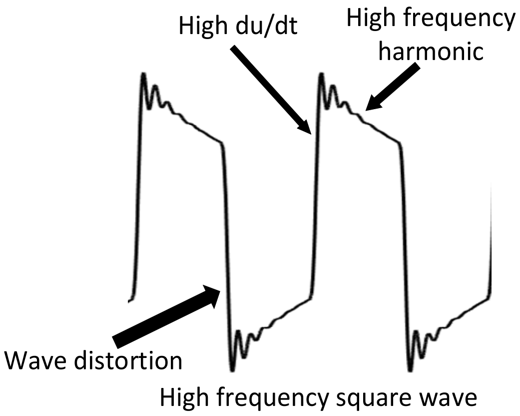

Figure 1. The typical winding voltage waveform of the high-frequency reactor in power electronic equipment.

There are three main methods for thermal research on the reactors: the mathematical calculation model, equivalent thermal network model and finite element model, investigated in [4–8]. The mathematical calculation is based on the mechanism of heat transfer. It is the basis of all types of heat research and is commonly used for hot spot temperature prediction. Based on the geometry and material properties of the reactor, the equivalent thermal network model is modeled by the thermal network method. The finite element model uses the finite difference method, which is usually performed by powerful simulation tools, such as COMSOL and ANSYS. Although these methods can illustrate the heat transfer mechanism of the reactor accurately, the finite element model needs more details and consumes more time. In contrast, the mathematical calculation model and the thermal network model can obtain the temperature features by solving some simple equations from divided nodes, and the latter is more accurate, which makes the thermal network model more practical.

Many studies have focused on the thermal analysis of magnetic devices, such as transformers, reactors and motors [9–14]. In [9], a transformer thermal network model based on nonlinear thermal resistance and the lumped heat capacity under the transient condition realizes the calculation of transformer temperature. The authors of [10] present a function of core loss and ambience based on the temperature simplified analytical equivalent thermal resistance of the planar transformer. A thermal model of inductor and transformer windings, including litz wire, was built in [11]. In another example, L. Wang et al. applied the dynamic thermal model with prephysical modeling for transformers in [12]. Additionally, the thermal network method and two-dimensional numerical simulation method were used to study the rotor temperature field distribution of the permanent magnet synchronous traction motor in [13]. Additionally, Eslamian et al. studied the temperature distribution of transformers and verified the simulation by experiments [14]. Although all of these methods can perform the thermal analysis of a magnetic device, they are either too complex or only consider one aspect of heat transfer in magnetic devices. Therefore, a new method, which is more explicit and calculates more rapidly, must be investigated for the thermal analysis of the reactors.

The focus of this paper is to build a thermal network model suitable for a reactor under high-frequency and high-power square wave voltage and to obtain the internal temperature rise hot spots of the reactor through the external temperature data, ambient temperature and material coefficient. The geometrical structure of the reactor is taken into account in the model, and its equivalent geometric heat transfer effect is obtained through three-dimensional thermal resistance. The surface thermal impedance method is applied to achieve an equivalent high-frequency thermal penetration effect, which is more accurate than the traditional model. The winding thermal resistance can be equivalent to multilayer cylindrical walls, and its equivalent conduction thermal resistance can be more quickly calculated than with other models. At the same time, the transient temperature variation of the reactor with time can be analyzed by using the lumped heat capacity method.

The paper is organized as follows: Section 2 includes the thermal analysis and thermal modeling of the reactor. In Section 3, the finite element model is used to simulate the temperature distribution of the reactor for comparison with the proposed thermal network model. Additionally, experimental verification and analysis are presented in Section 4.

2. The Thermal Network Model of the Reactor

2.1. Conventional Temperature Model

The traditional temperature model of the reactor assumes that its cooling rate is approximately proportional to the radiant area of its surface. The core loss and winding loss are taken as the total loss. Under the equilibrium state, all the energy generated inside the reactor is transferred to the outside through the surface radiation area. Among this, 45% is transmitted outward through heat conduction and 55% through heat radiation. The temperature rise of the reactor under the equilibrium state can be expressed as [15]:

$$\Delta T = 450\psi^{0.826} = 450(P_{CW}/A_t)^{0.826} \tag{1}$$

where A_t is the radiation surface and P_{CW} is the sum of core loss and winding loss. This model can only calculate the average temperature rise of the reactor, but not obtain the temperature hot spot, and it ignores the influence of the high-frequency effect and three-dimensional geometric effect. Therefore, it is not a suitable method for thermal analysis of high-frequency and high-power reactors.

2.2. Heat Transfer Analysis

There are generally three ways of heat transfer: conduction, convection and radiation [16]. Thermal resistance is usually used in heat propagation models such as heat conduction and heat convection. The thermal resistance of heat conduction in a monolayer material is

$$R_{cond} = \frac{l}{k_c A} \tag{2}$$

where l is the length, A is heat transfer area and k_c is the thermal conductivity.

The thermal resistance in the process of thermal convection can be expressed as

$$R_{conv} = \frac{1}{hA} \tag{3}$$

where h represents the thermal convection coefficient.

Thermal radiation thermal resistance can be expressed as

$$R_{rad} = \frac{1}{\alpha_{rad} A} \tag{4}$$

where α_{rad} represents the thermal radiation coefficient.

The conduction heat resistance of the winding can be equivalent to multilayer cylinders. As shown in Figure 2a, the cylindrical coordinate system is tantamount to the heat transfer of the winding to one-dimensional heat conduction along the radius direction [17]. Then, the equivalent thermal resistance of the winding can be expressed as

$$R_{\Phi} = \frac{\ln(r_2/r_1)/a_1 + \ln(r_3/r_2)/a_2 + \ln(r_4/r_3)/a_3}{2\pi l_h} \tag{5}$$

where the definitions of each parameter are shown in Figure 2a.

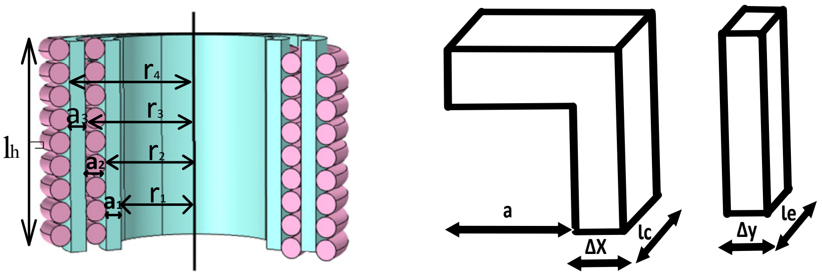

(**a**) (**b**)

Figure 2. (**a**) Schematic diagram of winding multi-layer cylinder; (**b**) Core structural parameters diagram.

The three-dimensional heat transfer of the core in the reactor can be simulated by the multidimensional steady-state conduction analysis method [18], but the analytical solution of the three-dimensional heat transfer equation is complicated. Based on the basic principle that the isotherm must be perpendicular to the heat flow line, the three-dimensional heat transfer effect of the core can be simulated through the shape factor, which can be equivalent to the multidimensional conduction heat resistance. The equivalent thermal resistance of it can be expressed as [19]:

$$R_{conv}(D) = \frac{1}{k_c S} \tag{6}$$

where S represents the shape factor, and

$$S = \begin{cases} 0.54 l_C & l_C > \Delta x \\ 0.15\Delta y & l_e > \Delta y \end{cases} \tag{7}$$

where the definitions of l_c, l_e, Δx and Δy are shown in Figure 2b.

It is necessary to consider the high-frequency effect on the thermal network modeling of the reactor. It can be modeled by the thermal surface impedance method. The heat source that causes the temperature rise of the core comes from two aspects. As shown in Figure 3, one is generated by the loss of the core, which affects the core directly. Another is the copper loss from the winding indirectly causes the temperature rise of the core through heat transfer. Here, we assume that the core is a plate of finite thickness. Hence, the high-frequency heatwaves generated by the core will decrease with the penetration depth from the inside to the outside. Additionally, the heat generated by the winding will decrease with the penetration depth from the outside to the inside. Moreover, the depth of thermal penetration can be calculated by the working frequency and thermal conductivity. Here, assuming that the thermal conductivity of the reactor is isotropic, the thermal surface impedance R_f of its core can be expressed as [20]:

$$R_f = \frac{1}{\sqrt{4\pi f C_p \rho k_c A}}\left[\frac{\sinh(2a) - \sin(2a)}{\mathrm{conh}(2a) - \cos(2a)}\right] \tag{8}$$

where f is frequency, C_p is heat capacity, ρ is density, a is a function of contact thickness, $a = d/\delta_{th}$, d is thickness and δ_{th} is depth of heat penetration. When the frequency becomes higher and the penetration depth becomes lower, the more uneven the temperature variation and the higher the temperature gradient become.

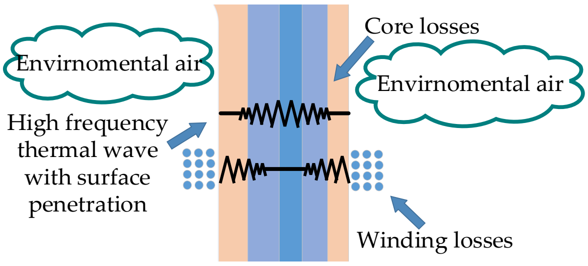

Figure 3. High-frequency heat flow depth of heat penetration.

Due to the high-frequency effect, the core loss includes hysteresis loss, the eddy current loss and the corresponding core loss for the reactor; it can be calculated by [21]:

$$P_{core} = kf^a B_m^b D^{b-a+1} \tag{9}$$

where k, a and b are the material correlation constants, respectively, B_m is the amplitude of magnetic induction intensity and D is the duty cycle.

When the high-frequency time-varying current flows through the reactor windings, they are in the magnetic field induced by the current of the neighboring conductor. The field can further induce eddies in the conductor, converting electromagnetic energy into heat energy. Furthermore, both the skin effect and proximity effect can make the high-frequency current density uneven in the conductor, which limits the conductor's ability to conduct high-frequency current. The winding copper loss can be obtained by the improved Dowell formula [22]:

$$P_{cu} = \left(\frac{\xi}{2}\frac{\sinh(\xi)+\sin(\xi)}{\cosh(\xi)-\cos(\xi)}R_{dc}\right)I_{rms}^2 \tag{10}$$

where I_{rms} is the effective value of the current, R_{DC} is the DC resistance of the winding, ξ is a constant that can be deduced by the function of conductor height h and skin depth δ as $\xi = h/\delta$.

The core loss and winding loss are used as heat sources to flow into each node of the thermal network model. Taking temperature as the quantity to solve, the heat balance equation is established for each unit or loop:

$$\sum_j \frac{f(T_n^{j+1}) - f(T_n^j)}{R_{j,n}} + P_n = 0 \tag{11}$$

where ${T_n}^{j+1}$ is the stable temperature of node $j + 1$, ${T_n}^j$ is the initial temperature of node j and P_n is the power flowing through node $j + 1$ and node j.

The heat balance equation can be written by the matrix expression

$$\begin{vmatrix} \frac{1}{R_{11}} & \frac{1}{R_{12}} & \cdots & \frac{1}{R_{1i1}} \\ \frac{1}{R_{21}} & \ddots & \ddots & \vdots \\ \vdots & \ddots & \ddots & \vdots \\ \frac{1}{R_{i1}} & \cdots & \cdots & \frac{1}{R_{ii}} \end{vmatrix} \begin{vmatrix} \Delta T_1 \\ \vdots \\ \vdots \\ \Delta T_i \end{vmatrix} = \begin{vmatrix} P_1 \\ \vdots \\ \vdots \\ P_i \end{vmatrix} \tag{12}$$

The temperature of each node can be obtained by solving Equation (12), which is the function of the loss in magnetic core and the loss of winding. Additionally, the corresponding expression is shown as follows:

$$\Delta T_i = x_i P_{core} + y_i P_{cu} \tag{13}$$

Finally, its time constant can be obtained based on the material parameters of the reactor. The temperature distribution of the high-frequency and high-power reactor with time can be computed by the lumped heat capacity method. Therefore, the time-dependent temperature can be calculated by

$$T = (T_0 - T_\infty)e^{(-\frac{t}{\tau})} + T_\infty \tag{14}$$

where T_i is the ambient temperature, T_∞ is the stable temperature and the time constant τ can be obtained by

$$\tau = \frac{\rho V_C C_P}{hA} \tag{15}$$

where ρ is the density of the magnetic core, V_c is the volume of the core, C_p is the heat capacity of the magnetic core and h is the thermal convection coefficient.

From the above analysis, the proposed thermal network can be built based on the shape of the magnetic core, winding structure and material specification.

2.3. The Reactor Thermal Network Model and Temperature Calculation

The structure of the tested reactor is shown in Figure 4, and the corresponding parameters are shown in Table 1.

(**a**) (**b**)

Figure 4. (**a**) Reactor to be tested; (**b**) Reactor core size.

Table 1. Reactor parameters.

Reactor Regulation L20A2M-0PH	Magnetic Core Ni-Zn Ferrite	Winding Copper	Insulation Polyester Film
Rated Current 20 A	Rated Temperature 100 °C	Frequency 0–50 kHz	Inductance 2 mH

Based on the analysis above, the proposed thermal model for the reactor can be obtained. Figure 5 is the equivalent circuit of the proposed model. Here, the mechanism of the different heat exchange, three-dimensional geometry effects, high-frequency thermal resistances and the equivalent thermal resistance of the winding are considered completely. The descriptions of nodes are listed in Table 2. The core and windings losses, red in Figure 5, are injected into the model as heat sources, similar to a current source. Note that, in Figure 5, P_{Core1}, P_{Core2}, P_{Core3} and P_{Core4} represent the core losses at the top, leftward, bottom and dextral core columns of the studied reactor, respectively, and P_{Cu1} and P_{Cu2} display the windings losses. Moreover, from Figure 5, in order to provide the proper balance with high accuracy and a small calculation, 12 nodes are considered in the proposed thermal model. These nodes are obtained by the proposed theoretical modeling and methodology.

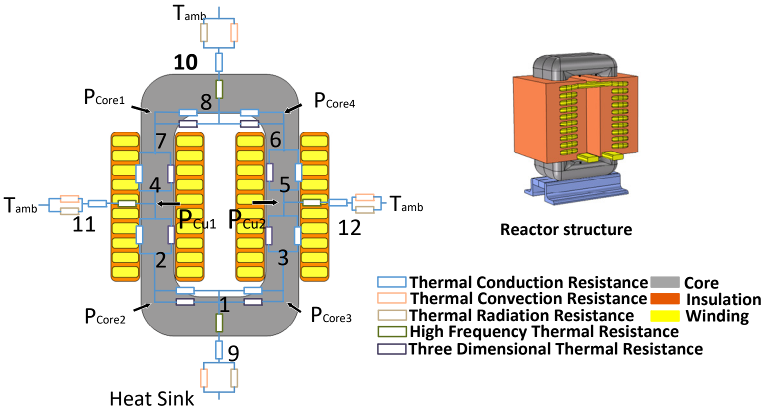

Figure 5. Equivalent thermal network model of reactor.

Table 2. Definition of each node.

Nodes		
1: Core bottom column	2: Core bottom left corner	3: Core bottom right corner
4: Core left column	5: Core right column	6: Core top right corner
7: Core top left corner	8: Core top column	9: Core bottom surface
10: Core top surface	11: Left winding surface	12: Right winding surface

According to the heat balance equation, the temperature of each node can be obtained by Equation (13). In order to simplify calculation, the temperature of nodes 1–8 can be solved firstly for reducing the order of the matrix. Additionally, the temperature of nodes 9–12 can be obtained indirectly by nodes 1–8. The calculation results of nodes 1–8 are shown in Table 3.

Table 3. Temperature calculation results of each node.

Node	$\mathbf{x_i}$	$\mathbf{y_i}$	**Node**	$\mathbf{x_i}$	$\mathbf{y_i}$
1	0.2224	0.1160	5	0.2851	0.1854
2	0.2356	0.1540	6	0.2558	0.1586
3	0.2356	0.1540	7	0.2558	0.1586
4	0.2851	0.1854	8	0.2312	0.1310

The temperature calculation results of nodes 9–12 are shown as follows:

$$\Delta T_{11,12} = 0.4167 \Delta T_{4,5} \tag{16}$$

$$\Delta T_{9} = 0.8142 \Delta T_{1} \tag{17}$$

$$\Delta T_{10} = 0.8498 \Delta T_{8} \tag{18}$$

3. Finite Element Simulation

In order to verify the accuracy of the thermal network model, the corresponding finite element simulation is built in this section. Finite element analysis is a more accurate simulation than the thermal network model for the heat transfer mechanism of the reactor. The advantage is especially obvious when the accurate model of three-dimensional geometry is established for calculating its operating temperature. However, the main disadvantage of the finite element analysis is that the calculation time is long, and the thermal and electromagnetic time constants are difficult to be coupled. Moreover, due to the high switching frequency, short step size and a large thermal time constant need to be considered in the transient electromagnetic simulation, so that the simulation model becomes a rigid system with multiple time scales.

The algorithm flow of the finite element modeling is shown in Figure 6. Considering the frequency-transient simulation, the thermal and magnetic finite element models can be coupled. To some extent, this method overcomes the simulation difficulties caused by multiple time scales.

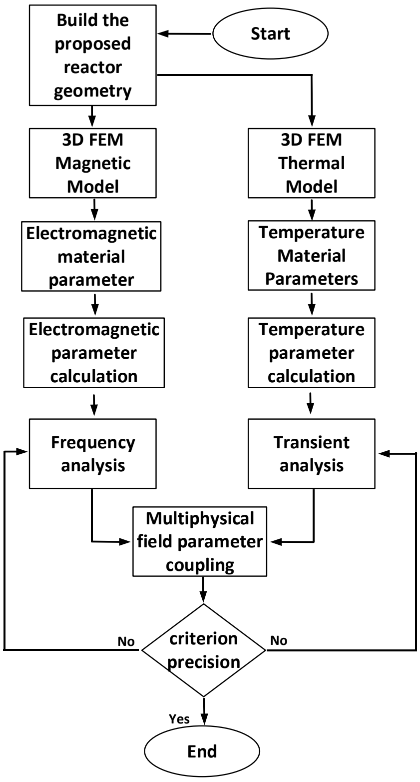

Figure 6. Finite element solution process.

The simulation adopts a three-dimensional model. Here, the components are composed of a finite element domain, magnetic core, winding and insulation. The finite element domain is air, the magnetic core material is nickel zinc ferrite, the winding is copper conductor and the insulating material is polyester film. Moreover, the physical field consists of an electromagnetic field and solid heat transfer. Note that the latter has the coupling developed by multiple physical fields. Additionally, the frequency-transient cosimulation is employed in this simulation, i.e., the electromagnetic field working in the frequency domain and the temperature field working in the transient state. The electromagnetic field equation is shown as follows:

$$\begin{cases} \nabla \times J = 0 \\ \nabla \times H = J \\ B = \nabla \times A \\ E = -\nabla \cdot V - j\omega A \\ J = \sigma E + j\omega D + \sigma v \times B + J_e \end{cases} \tag{19}$$

where J is the conduction current density, H is the magnetic field intensity, B is the magnetic flux density, E is the electric field intensity, V is the electric potential, ω is the angular frequency, σ is the electrical conductivity, D is the electric flux, J_e is the displacement current density and A is the vector magnetic potential.

The temperature field equation is

$$\begin{cases} \rho C_p \cdot \nabla T + \nabla \cdot q = Q + Q_{\text{ted}} \\ q = -k\nabla T \end{cases} \tag{20}$$

where ρ is material density, C_p is material heat capacity, q is heat flux, Q is heat increment, Q_{ted} is initial heat and ∇T is temperature rise.

The finite element mesh model of the reactor is shown in Figure 7. The skin effect of the winding is analyzed by the boundary layer mesh at high frequency. Fine mesh and coarse mesh are used to manage simulation time with higher precision. However, the total number of finite element mesh nodes is still about 400,000, which will lead to a huge computational cost. This is a disadvantage of finite element modeling.

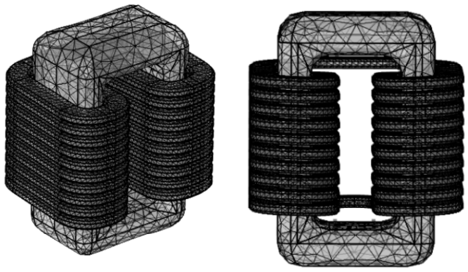

Figure 7. Reactor mesh generation.

The simulation parameters are shown in Table 4, which adopt the SI International System of Units. Here, subscripts w, e and p represent windings, insulation and magnetic core, respectively.

Table 4. Finite element simulation parameters.

Item	V	f	σ_w	C_p	ρ_w	$\mathbf{T_0}$
Value	550	20,000	5.998×10^7	385	8940	293.15
Item	σ_c	$\boldsymbol{\mu}_c$	σ_e	ρ_c	ρ_e	ε
Value	526	800	0.004	8600	1393	1
Item	k_c	k_w	k_e	C_w	C_e	
Value	152	400	0.8	386	0.27	

The finite element simulation results are shown in Figure 8. Here, the maximum flux density is 0.35 T, and the flux density fastens to the magnetic core. This strong magnetic field will have an impact on the measurement accuracy of some sensors with weak anti-interference. According to the results of the temperature field, the temperature distribution of the winding is low in the middle and high in the upper and lower, which is related to the uneven distribution of the winding voltage caused by the fast-rising edge and falling edge. Moreover, the temperature hot spots of the magnetic core focus on the center of the left and right magnetic core columns because of the short magnetic circuit at this position and the poor heat dissipation under the winding.

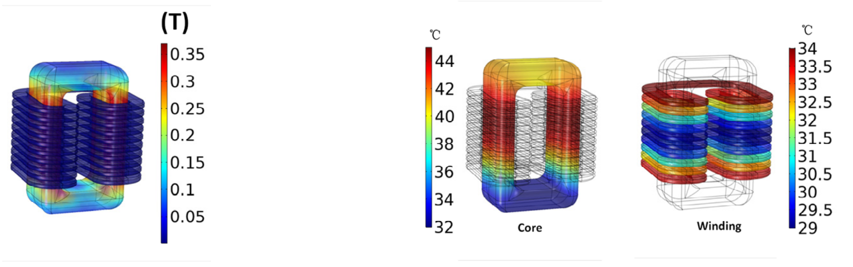

(**a**) (**b**)

Figure 8. (**a**) Simulation results of electromagnetic field; (**b**) Simulation results of temperature field.

4. Experimental Verification

4.1. Construction of Experimental Platform

In order to verify the proposed thermal network model, a corresponding experimental platform was built based on the studied reactor. The experimental circuit is shown in Figure 9.

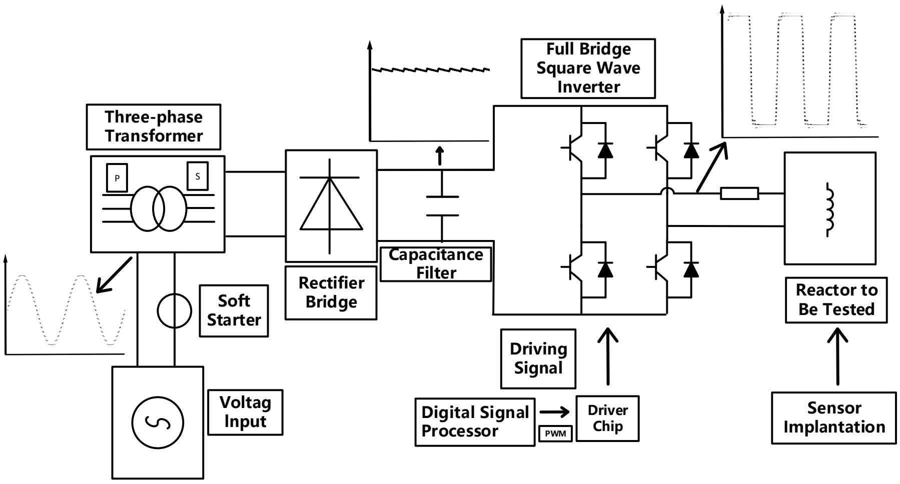

Figure 9. Experimental circuit and waveforms. DSP: (Digital Signal Processor).

The established experimental platform is shown in Figure 10. Here, the important components are labeled.

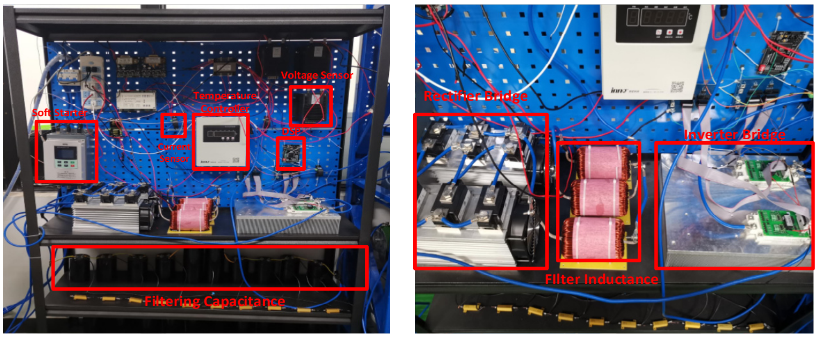

Figure 10. Experimental facility.

Due to the effect of the strong magnetic field inside the reactor, the traditional thermocouple temperature measurement will produce eddy current in the probe, which will affect the measurement accuracy. Therefore, the optical fiber sensor is utilized for higher precision, which does not need an electrical connection between the sensor and the receiving part. The designment, weakening the influence of the strong electromagnetic interference, can measure the temperature accurately. Note that according to the finite element simulation results and the thermal network model, the optical fiber temperature sensor is implanted into the corresponding temperature hot spot of the reactor to achieve a more accurate temperature measurement.

4.2. Experimental Analysis

Under the condition of ±550 V, ±750 V and ±1050 V square wave with frequency of 20 kHz and ambient temperature of 20 °C, we measured the stable temperature of the reactor. According to Equations (10) and (11), the corresponding trend of core loss and winding loss with voltage change are shown in Figure 11. Fiber optic sensor probes are implanted in nodes 2, 4, 5, 10, 11 and 12 of the reactor, respectively. The temperatures of nodes 1, 3, 6, 7, 8 and 9 are indirectly calculated by the corresponding thermal network model. In addition to the application of the optical fiber sensor, this paper also uses an infrared thermal imager to measure the reactor temperature, as shown in Figure 12. The infrared thermal imager can measure the external three-dimensional temperature distribution of the reactor, but it cannot directly measure the internal temperature of the reactor. Figure 13 displays the comparisons of temperature measurement and the thermal network model and finite element model.

From the experimental results, we can see that the thermal network model has the highest accuracy. When the voltage is ±550 V, ±750 V and ±1050 V, the error is 3.8%, 3.1% and 2.4%, respectively. The error decreases as the temperature increases. It is shown that this method is an effective method for overtemperature protection of the reactor. The finite element model has high accuracy, and its result is very close to the experimental results, but it requires a significant amount of calculation time.

Figure 14 shows the comparison among the proposed model, the model without high-frequency thermal resistance, the model without three-dimensional thermal resistance and the experiment result when the voltage is ±1050 V. When the high-frequency thermal resistance is ignored, the temperature of each node will be lower than the experimental result, and the degree of temperature inequality is more evident. When three-dimensional thermal resistance is disregarded, the temperature of each node obtained by the thermal network model is larger than the experimental result due to the neglect of the three-dimensional geometric cooling effect of the reactor. It is obvious that the proposed model has a higher accuracy and considers the influence of different factors on heat transfer. Therefore, under the premise of convenient calculation, the proposed model is more suitable for temperature prediction of the reactor.

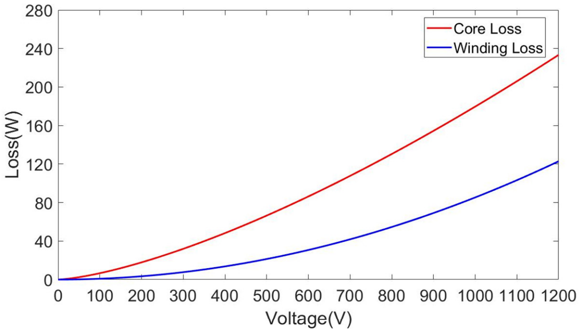

Figure 11. The trend of core loss and winding loss with voltage changing.

Figure 12. Experimental temperature distributions of the studied reactor under the thermal steady-state condition when voltage is ±1050 V.

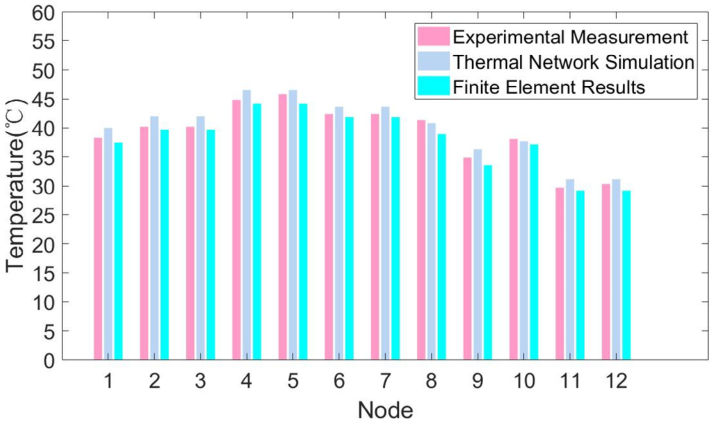

(**a**)

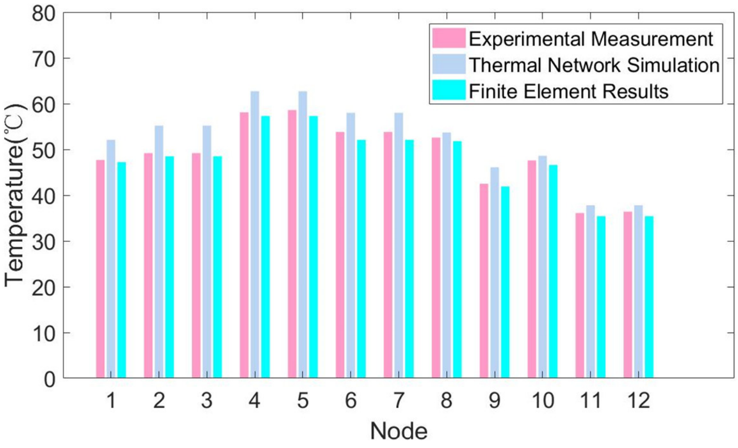

(**b**)

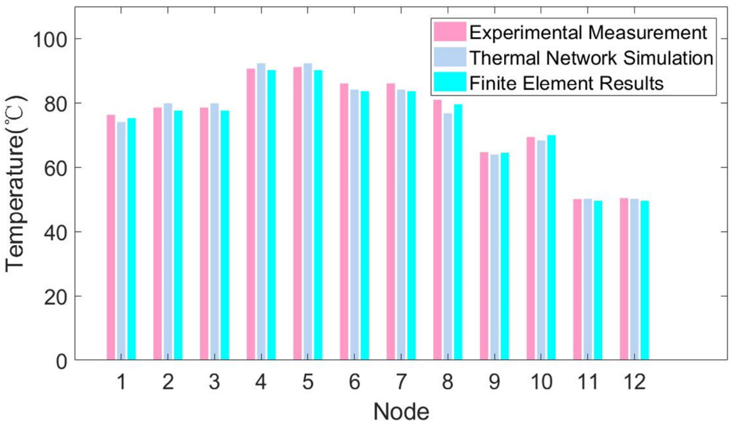

(**c**)

Figure 13. Steady-state temperature of each reactor node: (**a**) ±550 V; (**b**) ±750 V; (**c**) ±1050 V.

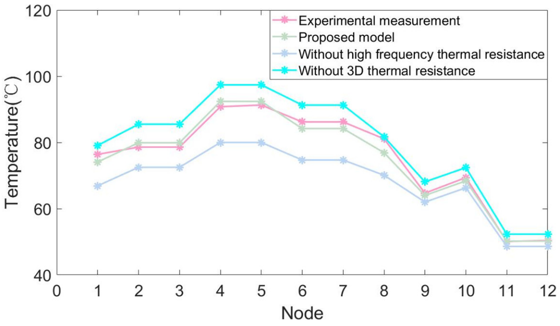

Figure 14. The comparison among the proposed model, the model without high-frequency thermal resistance, the model without three-dimensional thermal resistance and the experimental result under the voltage of ±1050 V.

Figure 15 shows the temperature variation of node 2 and node 4 with time under the voltage of 750 V. The experimental results show that the heat capacity model has the excellent ability of determining temperature rise, and the average error between the temperature rise curve calculated by the heat capacity model and the actual measurement is about 2.2%.

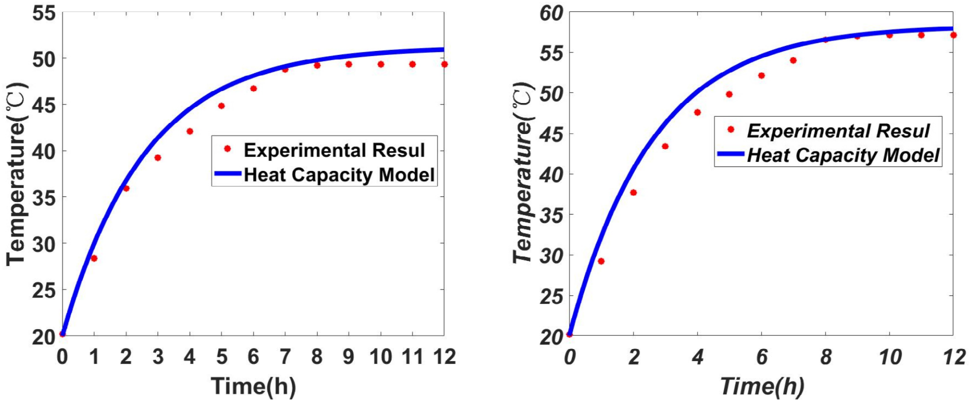

(**a**) (**b**)

Figure 15. Transient curve of node temperature: (**a**) Node 2; (**b**) Node 4.

From the above analysis, both the thermal network model and the finite element model can be used for thermal analyses of the reactor. The finite element model has a higher accuracy; nevertheless, the finite element modeling is complex and requires a significant amount of calculation time. The calculation time of the above finite element model is about 44 h when the degree of freedom is 40,000, and the computer parameters are Intel Core i7-8750H, NVIDIA GTX10606G GDDR5 and 16 GB DDR4. Additionally, the thermal network model can quickly calculate the stable temperature of each reactor node, which is a very practical method for both initial thermal design and analysis of heat transfer characteristics.

5. Conclusions

This paper has focused on building an improved thermal network model for reactors under high-frequency and high-power conditions. According to the different heat transfer mechanisms, we obtained the corresponding heat transfer resistances. The thermal model of the reactor was divided into multiple nodes, and a suitable thermal network model of the reactor was built. Compared with the traditional equivalent model, this method can calculate the temperature of different nodes in the reactor more accurately and quickly. In addition, the lumped heat capacity model is used to analyze the transient heat of the reactor for obtaining its temperature variation with time. Finite element modeling and experimental tests are carried out to verify the validation of the proposed model. The simulation results and experimental results show that the thermal network model has a high accuracy, the error of results between the experimental and the model being about 3%, and the accuracy increases with the rise of temperature. Through the application of this model, the internal temperature hot spot can be calculated by measuring the external temperature of the reactor. Therefore, it is an effective method to obtain the reactor temperature hot spot.

Consequently, the main advantages of the proposed thermal network model include a low computational time and high effectiveness and accuracy for both steady-state and transient thermal analyses.

Author Contributions: Conceptualization, L.S. and F.X.; methodology, L.S.; software, L.S.; validation, L.S., F.X. and B.Z.; formal analysis, L.S.; investigation, L.S.; data curation, H.J.; writing—original draft preparation, L.S.; writing—review and editing, H.J.; supervision, W.X.; project administration, F.X.; funding acquisition, F.X. All authors have read and agreed to the published version of the manuscript.

Funding: This research was funded by the National Key Research and Development Program of China, grant number 2018YFB0905803.

Informed Consent Statement: Informed consent was obtained from all subjects involved in the study.

Conflicts of Interest: The authors declare no conflict of interest.

References

1. Nasser, H.; Asma, A. Voltage Stability of Power Systems with Renewable-Energy Inverter-Based Generators: A Review. *Electronics* **2021**, *10*, 115.
2. Li, C.; Gole, A.M.; Zhao, C. A Fast DC Fault Detection Method Using DC Reactor Voltages in HVDC Grids. *IEEE Trans. Power Deliv.* **2018**, *33*, 2254–2264. [CrossRef]
3. Liu, G.H.; Zhang, Y.N.; Chen, Z.L.; Jia, H.P. PMSM DTC predictive control system using SVPWM based on the subdivision of space voltage vectors. In Proceedings of the 2009 IEEE 6th International Power Electronics and Motion Control Conference, Wuhan, China, 17–20 May 2009; pp. 1818–1821.
4. Li, H.Y.; He, M.; Huang, L. Correlation between the Generation of Acidic Products and the Thermal Aging of Oil-paper Insulation of the UHV Transformer. *High Volt. Eng.* **2015**, *6*, 1959–1964.
5. Ghahfarokhi, P.S.; Kallaste, A.; Vaimann, T. Steady-State Thermal Model of a Synchronous Reluctance Motor. In Proceedings of the 2018 IEEE 59th International Scientific Conference on Power and Electrical Engineering of Riga Technical University (RTUCON), Riga, Latvia, 12–14 November 2018; pp. 1–5.
6. Guo, Y.G.; Zhu, J.G.; Wu, W. Thermal analysis of soft magnetic composite motors using a hybrid model with distributed heat sources. *IEEE Trans. Magn.* **2005**, *41*, 2124–2128.
7. Santisteban, A.; Piquero, A.; Ortiz, F.; Delgado, F.; Ortiz, A. Thermal Modelling of a Power Transformer Disc Type Winding Immersed in Mineral and Ester-Based Oils Using Network Models and CFD. *IEEE Access* **2019**, *7*, 174651–174661. [CrossRef]
8. Liu, C.; Ruan, J.J.; Liang, S.Y. Improvement of Transformer Air Duct with Thermal-fluid Coupled Field Simulation by FEM. *Water Resour. Power* **2016**, *34*, 195–198.
9. Górecki, K.; Detka, K.; Górski, K. The Nonlinear Compact Thermal Model of the Pulse Transformer. In Proceedings of the 25th International Workshop on Thermal Investigations of ICs and Systems (THERMINIC), Lecco, Italy, 25–27 September 2019; pp. 1–4.
10. Sayani, M.P.; Skutt, G.R.; Venkatraman, P.S. Electrical and thermal performance of PWB transformers. In Proceedings of the APEC '91: Sixth Annual Applied Power Electronics Conference and Exhibition, Dallas, TX, USA, 10–15 March 1991; pp. 533–542.
11. Kyaw, P.A.; Delhommais, M.; Qiu, C. Thermal Modeling of Inductor and Transformer Windings Including Litz Wire. *IEEE Trans. Power Electron.* **2020**, *35*, 867–881. [CrossRef]
12. Wang, L.; Zhou, L.; Yuan, S. Improved Dynamic Thermal Model With Pre-Physical Modeling for Transformers in ONAN Cooling Mode. *IEEE Trans. Power Deliv.* **2019**, *34*, 1442–1450. [CrossRef]
13. Jaritz, M.; Biela, J. Analytical model for the thermal resistance of windings consisting of solid or litz wire. In Proceedings of the 2013 15th European Conference on Power Electronics and Applications (EPE), Lille, France, 2–6 September 2013; pp. 1–10.
14. Eslamian, M.; Ahidi, V.; Eslamian, B.A. Thermal analysis of cast-resin dry-type transformers. *Energy Convers.* **2011**, *52*, 2479–2488. [CrossRef]
15. Marian, K.K. *High-Frequency Magnetic Components*, 2nd ed.; Wiley: Hoboken, NJ, USA, 2013; pp. 293–296.
16. Yang, S.M.; Tao, W.Q. *Heat Transfer*, 4th ed.; Higher Education Press: Beijing, China, 2006; pp. 4–12.

17. Jain, A.; Jones, R.E.; Chatterjee, R.; Pozder, S. Analytical and Numerical Modeling of the Thermal Performance of Three-Dimensional Integrated Circuits. *IEEE Trans. Compon. Packag. Technol.* **2010**, *33*, 56–63. [CrossRef]
18. Bergman, T.L.; Lavine, A.S.; Incropera, F.P.; Dewitt, D.P. *Fundamentals of Mass and Heat Transfer*, 7th ed.; Wiley: Hoboken, NJ, USA, 2011; pp. 46–78.
19. Shafaei, R.; Ordonez, M.; Saket, M.A. Three-Dimensional Frequency-Dependent Thermal Model for Planar Transformers in LLC Resonant Converters. *IEEE Trans. Power Electron.* **2019**, *34*, 4641–4655. [CrossRef]
20. D'Esposito, R.; Balanethiram, S.; Battaglia, J.; Frégonèse, S.; Zimmer, T. Thermal Penetration Depth Analysis and Impact of the BEOL Metals on the Thermal Impedance of SiGe HBTs. *IEEE Electron Device Lett.* **2017**, *38*, 1457–1460. [CrossRef]
21. Chen, J.; Ma, J.; Fang, Y. An Improved Steinmetz Premagnetization Graph (SPG) Applied in High Magnetic Field. In Proceedings of the 22nd International Conference on Electrical Machines and Systems (ICEMS), Harbin, China, 11–14 August 2019; pp. 1–5.
22. Whitman, D.; Kazimierczuk, M.K. An Analytical Correction to Dowell's Equation for Inductor and Transformer Winding Losses Using Cylindrical Coordinates. *IEEE Trans. Power Electron.* **2019**, *34*, 10425–10432. [CrossRef]